Photocatalytic Performance Enhancement of Carbon Nitride Aerogel via Oxygen-doping

Wenjun Jiang,[a] Qiushi Ruan,[b] Jijia Xie,[b] Xianjie Chen,[a] Yongfa Zhu*[a] and Junwang Tang*[b]

Abstract: Oxygen-doped carbon nitride aerogel (OCNA) was successfully fabricated through a facile self-assembly method combined with hydrothermal process, without adopting any harmful solvents or cross-linking agents. The assembly mechanism of carbon nitride aerogel (CNA) with different morphologies was discussed. OCNA exhibited much faster charge separation efficiency, longer carriers' lifetime than bulk carbon nitride (BCN). More importantly, oxygen-doping adjusted the band structure of carbon nitride, leading to a more negative conduction band (CB) position and narrower band gap (E_g). The spectral response range of OCNA was extended greatly and the hydrogen evolution rate (HER) of OCNA ($\lambda > 510$ nm) was about 26 times as high as that of BCN prepared herein. The apparent quantum yield (AQY) was 20.42% at 380 nm, 7.43% at 420 nm and 1.71% at 500 nm. This work paves a facile colloid chemistry strategy to assemble 3D CAN that could be widely adopted in the sustainability field.

Energy and environmental issues seriously constrain the sustainable development of human society. Photocatalysis has been regarded as one of the most promising techniques to solve these problems owing to its characteristic of stable, low cost, nontoxic and efficient harvesting of solar energy[1]. To date, various photocatalytic materials have been developed from UV-driven photocatalysts represented by TiO_2 to visible-light-driven photocatalysts represented by CdS[2]. Unfortunately, the band structures of these inorganic semiconductors could hardly be changed restricted by their intrinsic crystal structure. Polymeric photocatalysts with delocalized conjugated π-system may be an excellent candidate to overcome these problems thanks to their tunable electronic structure. A series of conjugated polymeric photocatalysts has been developed[3], such as graphite carbon nitride (g-C_3N_4, or CN)[4], 1,3,5-tris-(4-ethynylphenyl)-benzene (TEPB)[5], covalent triazine frameworks[6], Poly(diphenylbutadiyne) (PDPB)[7], among which g-C_3N_4 is one of the most excellent polymeric photocatalysts thanks to the appropriate band position and facile synthetic methods.

So far, CNs with various morphologies from 0D, 1D, 2D to 3D have been designed[8], among which carbon nitride aerogel (CNA) or hydrogel (CNH) with 3D hierarchical structure are one of the most outstanding candidates thanks to their interconnected open-framework that could expose more reactive sites, provide convenient mass transfer channels and then promote the surface chemical reaction. Aiming at this goal, different strategies have been presented. For instance, Liu et al. reported a CN based hydrogel using poly(N-isopropylacrylamide) as cross-linking agents.[9] Yan et al. fabricated CN hydrogels with the aid of ionic Liquid.[10] Our group also reported the synthesis of polyaniline/CN hydrogel using polyaniline as cross-linking agents.[11] Unfortunately, all the above methods need cross-linking agents to act as supporting materials and self-supported CNA is rarely reported. Recently, Qu et al. presented a facile self-assembly method to synthesis self-supported CNA for the first time without adopting cross-linking agents.[12] This is a big breakthrough. However, the use of potassium thiocyanate as solvent may not be so eco-friendly. Therefore, a more environment-friendly method for the construction of self-supported CNA is still urgently needed.

Here, we report the synthesis of OCNA via a facile self-assembly method combined with hydrothermal process, without adopting any harmful solvents or cross-linking agents (Scheme S1). Figure 1a illustrates the hydrothermal tailoring process of BCN. Under high temperature and pressure, H_2O would act as a scissor tailoring the polymeric CN framework to small units. -H of H_2O was connected to the bridged tertiary nitrogen N-$(C)_3$ and -OH of H_2O was connected to the sp2-hybridized carbon (N-C=N) of the aromatic ring. As hydrothermal time increases, the degree of tailoring increases. Part of the bridged tertiary nitrogen will be converted to NH_3, which can be smelt when opening the autoclave. When hydrothermal time increases, the pH of CNH also increases (Figure S1), which indicates that there are more amino groups in the system. More hydroxyl and amino groups will be benefit for the dispersion of the samples. The Tyndall effect could be observed when the red laser passes the transparent sol solution (Figure S1), which demonstrates the formation of sol solution. Cotton-like ultra-light white aerogel with higher specific surface area could be obtained when the as-prepared CNH was directly dehydrated via a freeze-drying process (Figure S1 and S2). Figure 1b-e shows the FESEM images of CNA with different hydrothermal time. When the hydrothermal time is 3h, the morphology of CNA is large sheet with regular geometry and the sheet thickness is in the micron level. When hydrothermal time is extended to five hours, both large sheet and rod-like structure could be observed and the surface of the sample is rougher. It can be speculated that the rod-like structure is formed by the breakage of the sheet-like structure. When hydrothermal time is extended to six hours, the morphology of CNA is structured trunk-shaped rod and the diameter is 1-3 μm. In order to investigate the detailed morphology, we furtherly observed the TEM of CNA-6 (Figure S3). It can be seen that the trunk-shaped rod is composed of nanofibers with a diameter of about 30 nm. Further extending

[a]   Dr. W. jiang, Dr. X. Chen, Prof. Y. Zhu
       Department of Chemistry, Tsinghua University
       Tsinghua University, Beijing 100084, China
       E-mail: zhuyf@mail.tsinghua.edu.cn
[b]   Dr. Q. Ruan, Dr. J. Xie, Prof. J. Tang
       Solar Energy & Advanced Materials Research Group, Department of Chemical Engineering, UCL
       Torrington Place, London, WC1E 7JE (UK)
   E-mail: junwang.tang@ucl.ac.uk

       Supporting information for this article is given via a link at the end of the document.
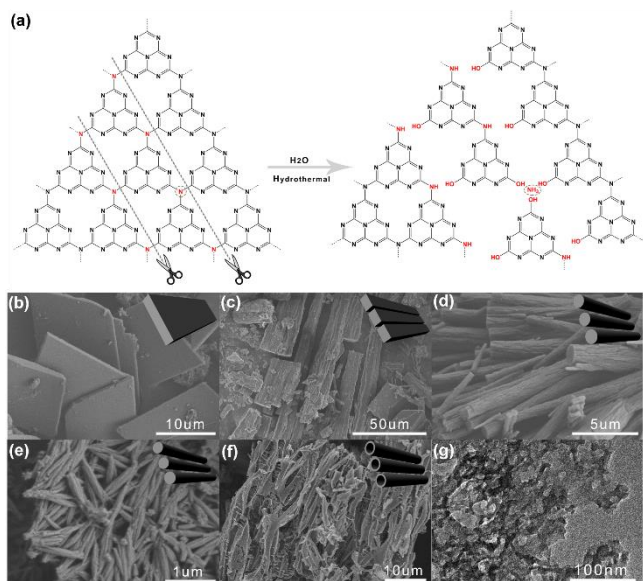
Figure 1. (a）Scheme of the hydrothermal tailoring process. (b-e) FESEM images of CNA-3, CNA-5, CNA-6 and CNA-12. (f) FESEM image of OCNA-6. (g) TEM images of OCNA-6.

Figure 2. (a) FT-IR spectra and (b) XRD patterns of different samples. (b) XPS and (c) solid-state ^{13}C NMR spectra of BCN and OCNA-6.

the hydrothermal time to 12 hours, the morphology of CNA is still structured trunk-shaped rod but with smaller diameter (0.3-0.5 μm). When calcining the CNA under N_2 atmosphere, CNA will re-polymerize into OCNA and the color of white aerogel turns back to yellow (Figure S1). As shown in Figure 1f, OCNA-6 exhibits a 3D hierarchical structure. Firstly, the hollow tubular structure makes up the 3D framework of the aerogel (Figure S4). Then, the hollow tubular structure is composed of dendritic nanofibers (Figure 1g). It can be speculated that the hollow tubular structure is the result of the re-polymerization of trunk-shaped rod in the calcining process since the volume will shrink during the process of dehydration condensation, which will be discussed later.

To further investigate the formation processes of the aerogels, the samples was characterized via FT-IR spectroscopy (Figure 2a). The peak at about 808 cm^{-1} represents the representative breathing mode of the CN heterocycles.[11] The peaks at 1200-1700 cm^{-1} represent the characteristic stretching vibration modes of the CN heterocycles.[12] The wide peaks in the region of 3000-3700 cm^{-1} represent the N-H and O-H stretching vibration.[12] Compared with the BCN, the peaks of CNA at this region exhibit stronger intensity demonstrating that there are more hydroxyl and amino groups, which indicates that the condensation was decreased.[13] A new peak at 1088 cm^{-1} was observed for CNA, which represents the C-O stretching vibration. When hydrothermal time increases, the intensity of the peak at 1088 cm^{-1} also increases indicating that there will be more hydrogen bonds between N-H and O-H. The hydrogen-bond interaction is quite important in the self-assembly process of CNA. The XRD pattern of CNA-6 is quite similar with that of melamine (Figure 2b), indicating that the BCN was tailored into melamine-based small molecular and the CNA was fabricated through the self-assembly of these small molecular. Scheme S2 illustrates the two possible self-assembly mechanism of CNA.
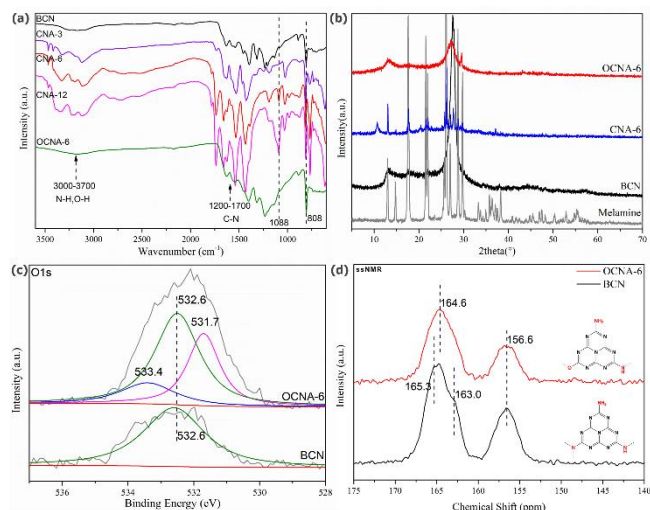
The hydrogen bonds may exist either between N-H and O-H or between O-H and O-H. In one direction parallel to the scheme, the intermolecular hydrogen bonding drives the self-assembly of the layers. In the direction perpendicular to the scheme, π-π interaction conducts the stacking of the layers. Figure 2b shows the XRD pattern, peak at 13.1° represents the (100) interplanar heptazine packing (d=0.68 nm) and peak at 27.5° represents the (002) interlayer π-π stacking (d= 0.33 nm).[14] Interestingly, a new peak for OCNA-6 was observed at 29.5° and the corresponding lattice plane spacing is 0.30 nm (Figure S4c). The reduced the interlayer π-π stacking distance could promote the charge transfer between the layers and from the bulk to the interface.[14] When the hydrothermal time is 3h, the morphology of CNA is large sheet with regular geometry. As the hydrothermal time increases, in another direction parallel to the scheme, part of the bridged tertiary nitrogen will be further cut off and the size of the sheet will get smaller. As the hydrothermal time is further extended, the sheet with smaller size will be converted to trunk-shaped rod. At last, the trunk-shaped rod will be converted to hollow tubular structure in the calcining process.

To further investigate the re-polymerization processes, the samples was characterized via XPS and solid-state ^{13}C NMR spectroscopy (Figure 2c and 2d). As shown in Figure 2c, the peak at 532.6 eV is attributed to the adsorbed H_2O.[11] Interestingly, two new peaks are found at 533.4 eV and 531.7 eV for OCNA-6 that represent C-O-C and C-OH, respectively.[15] Therefore, we can speculate that oxygen-doping was introduced during the re-polymerization. Scheme S2 illustrates the detailed formation process of oxygen-doping. H_2O will be removed in the hydrogen bonds between two molecular under high temperature. Then the bridged tertiary nitrogen will be replaced by oxygen and oxygen-doping is introduced. In the C1s spectra (Figure S5a and S5c), three peaks at 284.8 eV, 286.4 eV and 288.3 eV could be observed. The peak at 284.8 eV is attributed to the carbon contaminations. Peak at 288.3 eV represents N=C-N and peak at 286.4 eV is assigned to C-O.[15] Compared with BCN,
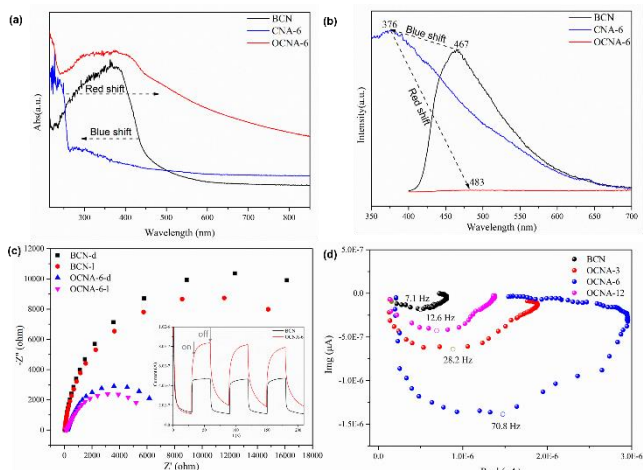
Figure 3. (a) DRS and (b) PL spectra of BCN, CNA-6 and OCNA-6. (d) photocurrent responses of BCN and OCNA-6 (insert: EIS Nyquist plots). (f) IMPS spectra of different samples at 0.8 $V_{Ag/AgCl}$.

the area ratio of the peak at 286.4 eV for OCNA-6 is much larger, indicating that the oxygen content of OCNA-6 is higher. In the N1s spectra (Figure S5b and S5d), three peaks are observed at 404.6eV, 400.9 eV and 398.8 eV, which are assigned to the positive charge localization effect, N-(C)$_3$ or –NH$_x$ and C=N-C, respectively.[11] Compared with BCN, the area ratio of the peak at 400.9 eV for OCNA-6 is much smaller, demonstrating that the bridged tertiary nitrogen content of OCNA-6 is decreased and part of the bridged tertiary nitrogen is replaced by oxygen. The atomic concentration of different samples is investigated via XPS in Table S1. Compare with BCN, the OCNA exhibits higher O and lower N concentration, demonstrating that oxygen-doping was successfully introduced. Interestingly, the degree of oxygen doping can be adjusted by hydrothermal time. As the hydrothermal time increases, the degree of oxygen doping also increases. Raman peak at 700 cm^{-1} represents the in-plane bending vibrations of the N-(C)$_3$ linked to heptazine units (Figure S6).[15] The peak of OCNA-6 at 700 cm^{-1} shows a red shift compared to BCN, which is also a supporting evidence of oxygen-doping. Solid-state ^{13}C NMR was also adopted to prove the presence of oxygen doping (Figure 2d). The peak at 153.6 ppm represents the C atom in CN$_3$[16], which could be observed in both BCN and OCNA-6 demonstrating that the basic heptazine was not destroyed during the hydrothermal treatment. For BCN, the peaks at 163.0 ppm and 165.3 ppm are assigned to the C atom in CN$_2$(NH) and CN$_2$(NH$_2$), respectively.[15] However, for OCNA-6, a new peak at 164.6 ppm could be observed representing the C atom CN$_2$(O),[15] , which is a conclusive evidence for the oxygen doping. Furthermore, it could be found that the peaks of BCN are broadened compared with OCNA-6, indicating that the structural disorder is increased. The increased structural disorder may be helpful for the band structure adjustment and the separation and transfer of photoinduced carriers.

To verify this point of view, the UV-Vis spectra were tested (Figure 3a). Compared with BCN, the absorption edge (λ_g) of CNA-6 exhibits a strong blue shift, which could be attributed to

the quantum size effect since BCN was tailored to smaller molecular.[17] After the re-polymerization, the absorption edge of OCNA-6 shows a strong red shift, indicating that the band gap narrows greatly. More importantly, the absorption intensity increases dramatically in both UV and Vis region, indicating that the light harvesting performance is promoted greatly. The enhanced light harvesting can be attributed to the 3D network structure, since the interconnected framework could increase the multireflection of the sun light.[8a] The flat-band potential and the band gap (Eg) can be evaluated by the Mott–Schottky plots and Tauc lots (Figure S7). The flat-band potential could be adopted to approximately evaluate the CB of n-type semiconductor.[18] Combine the values of CB and Eg, the valence band (VB) value will be determined. The band structure alignments are shown in Figure S7f and Table S2. The CB of OCNA-6 is more negative than that of BCN, indicating that OCNA-6 may show a stronger reduction ability for photoinduced electrons. The VB of OCNA-6 is less positive than that of BCN, which also could be confirmed by the XPS valence band spectra (Figure S7e). Both the position of CB and VB for OCNA-6 are eligible for the photocatalytic hydrogen or oxygen evolution.[19]

The photoluminescence (PL) spectra exhibits the similar phenomenon with the UV-Vis spectra. As shown in Figure 3b, BCN exhibits a sharp peak at about 467 nm. The peak of CNA-6 shows an obvious blue shift to 376 nm and the PL intensity is much stronger, which indicates that the photoinduced electrons and holes recombine more easily and goes against the photocatalytic reaction.[14, 20] After the re-polymerization, the PL peak of OCNA-6 shifts back to about 483 nm and the PL intensity is extremely weak, demonstrating that the electron-hole recombination rate for OCNA-6 is much lower than that of BCN.[14, 20] To further verify this point of view, the time-resolved PL was conducted (Figure S8). The emission peaks determine the mean radiative lifetimes (τ) of the photoinduced carriers (Table S3). The PL lifetime reflects the time for photoinduced carriers to decay to their "1/e" by radiative recombination. Hence,
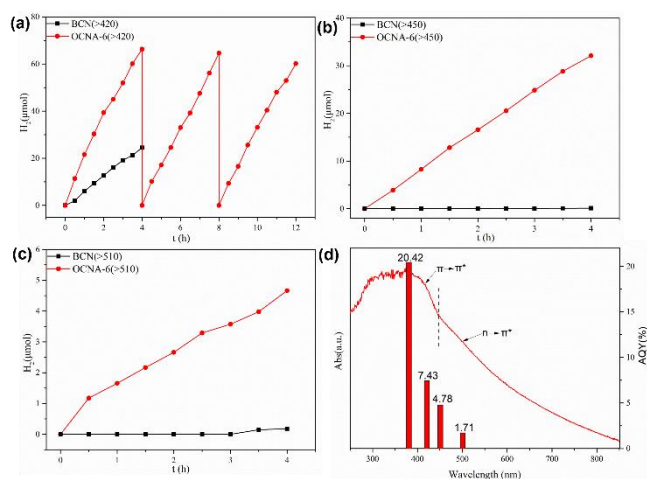
Figure 4. HER of BCN and OCNA-6 (a) $\lambda > 420$ nm, (b) $\lambda > 450$ nm and (c) $\lambda > 510$ nm. (d) wavelength-dependent AQY (right axis) and DRS (left axis) of OCNA-6.

longer PL lifetime represents slower charge recombination.[21] The τ for BCN and OCNA-6 is 8.715 ns and 13.365 ns, respectively. The remarkable prolonged PL lifetime for OCNA-6 indicates that the charge recombination is retarded and charge transfer is more efficient. Furthermore, the enhanced charge transport could be confirmed by the reduced hemicycle radius electrochemical impedance spectra (EIS, Figure 3c), which reflects the electric resistance of OCNA-6 is much slower.[14] The photocurrent response for OCNA-6 is approximately 1.8 times as high as that of BCN, proving that the transfer of the photoinduced carriers is promoted (insert of Figure 3c). Interestingly, when the light is off, the photocurrent of BCN decreases to zero quickly while the photocurrent of OCNA-6 exhibits an obvious delay, indicating that recombination of photoinduced carriers is hindered and the lifetime is prolonged greatly. Intensity modulated photocurrent spectroscopy (IMPS) is used to evaluate the charge transport performance (Figure 3d). The transit time (τ_D) could be obtained by $\tau_D=(2\pi f_{max})^{-1}$, which represents the average time photoinduced electrons need to reach the back contact.[22] f_{max} is the frequency where the minimum in the IMPS plot occurs. The f_{max} and τ_D of different samples are listed in Table S4. The τ_D of BCN is 22.4 ms while τ_D of OCNA-6 is only 2.2 ms, demonstrating that OCNA-6 possesses a much faster electron transfer rate and thus promotes the photocurrent density.

It is reasonable to speculate that the OCNA will exhibit an excellent HER performance thanks to the appropriate band location and outstanding charge separation and migration efficiency. With the increase of the re-polymerization temperature, the HER is also increasing (Figure S9). However, when the temperature over 550 °C, the sample will be carbonized. As shown in Figure 4a, the HER of OCNA-6 (16.57 µmol/h) is about 3 times as high as that of BCN (6.12 µmol/h/g) when λ>420 nm. Cyclic experiments were carried on to test the stability of OCNA-6 under the same conditions. The HER showed almost no decay after three cycles. The XRD (Figure S10) further demonstrates the stability of OCNA-6. When changing the wavelength (λ>450 nm, Figure 4b), the HER of OCNA-6 (8.02 µmol/h) is about 8 times as high as that of BCN (1.01 µmol/h/g). Further extending the wavelength (λ>510 nm, Figure 4c), the HER of OCNA-6 (1.17 µmol/h/g) is about 26 times as high as that of BCN (0.045 µmol/h/g) and BCN showed no hydrogen evolution in the first three hours. The longer the wavelength, the more obvious the difference in performance is (Figure S11). Therefore, it can be concluded that the spectral response range of OCNA was extended dramatically. The absorption band less than 445 nm is ascribed to the general π→π* electron transition of the conjugated system while the new absorption band more than 445 nm is attributed to the n→π* electron transition of the lone pairs in the edge N atoms (Figure 4d).[14] The n→π* electron transition is benificial for the utilization of visible light with longer wavelengths. Figure 4d exhibits the apparent quantum yield (AQY) of OCNA-6, which is well matched with the DRS. The AQY is 20.42% (380 nm), 7.43% (420 nm), 4.78% (450 nm) and 1.71% (500 nm), which is competitive compared with the recent literatures (Table S5).

The enhanced photocatalytic performance owes to the following reasons: Firstly, the interconnected open-framework of aerogels could expose more reactive sites, provide convenient mass transfer channels and then promote the surface chemical reaction. Secondly, oxygen-doping adjusts the band structure of carbon nitride, resulting in a more negative CB and extended spectral response range. More importantly, oxygen-doping facilitates the charge separation and migration efficiency and prolongs the lifetime of photoinduced carriers, resulting in a higher H_2 evolution rate. In summary, we successfully fabricate oxygen-doped carbon nitride aerogel via a facile self-assembly method combined with hydrothermal process, without adopting any harmful solvents or cross-linking agents. This eco-friendly method paves a facile colloid chemistry strategy to assemble 3D CAN that could be widely adopted in the sustainability field.

[1]   Q. Wang, T. Hisatomi, Q. Jia, H. Tokudome, M. Zhong, C. Wang, Z. Pan, T. Takata, M. Nakabayashi, N. Shibata, Nature Mater 2016, 15, 611-615.
[2]   aB. Qiu, M. Xing, J. Zhang, J Am Chem Soc 2014, 136, 5852-5855; bY. Xu, Y. Ye, T. Liu, X. Wang, B. Zhang, M. Wang, H. Han, C. Li, J. Am. Chem. Soc 2016, 138, 10726-10729; cK. K. Sakimoto, A. B. Wong, P. Yang, Science 2016, 351, 74-77; dH. Hirakawa, M. Hashimoto, Y. Shiraishi, T. Hirai, J Am Chem Soc 2017, 139, 10929-10936.
[3]   G. Zhang, Z. A. Lan, X. Wang, Angew Chem Int Edit 2016, 55, 15712-15727.
[4]   aX. Wang, K. Maeda, A. Thomas, K. Takanabe, G. Xin, J. M. Carlsson, K. Domen, M. Antonietti, Nature Mater 2009, 8, 76-80; bR. Godin, Y. Wang, M. A. Zwijnenburg, J. Tang, J. R. Durrant, J Am Chem Soc 2017, 139, 5216-5224; cV. W. h. Lau, D. Klose, H. Kasap, F. Podjaski, M. C. Pignié, E. Reisner, G. Jeschke, B. V. Lotsch, Angew Chem Int Edit 2017, 56, 510-514; dH. Yu, R. Shi, Y. Zhao, T. Bian, Y. Zhao, C. Zhou, G. I. Waterhouse, L. Z. Wu, C. H. Tung, T. Zhang, Adv Mater 2017, 29, 1605148.
[5]   L. Wang, Y. Wan, Y. Ding, S. Wu, Y. Zhang, X. Zhang, G. Zhang, Y. Xiong, X. Wu, J. Yang, Adv Mater 2017, 29, DOI: 10.1002/adma.201702428.
[6]   aP. Kuhn, M. Antonietti, A. Thomas, Angew Chem 2008, 47, 3450; bK. Schwinghammer, S. Hug, M. Mesch, J. Senker, B. V. Lotsch, Energ Environ Sci 2015, 8, 3345-3353.
[7]   S. Ghosh, N. A. Kouamé, L. Ramos, S. Remita, A. Dazzi, A. Deniset-Besseau, P. Beaunier, F. Goubard, P.-H. Aubert, H. Remita, Nature Mater 2015, 14, 505-511.
[8]   aW. Jiang, Y. Zhu, G. Zhu, Z. Zhang, X. Chen, W. Yao, J Mater Chem A 2017, 5, 5661-5679; bW. Jiang, W. Luo, J. Wang, M. Zhang, Y. Zhu, J Photoch Photobio C 2016, 28, 87-115.
[9]   J. Liu, T. An, Z. Chen, Z. Wang, H. Zhou, T. Fan, D. Zhang, M. Antonietti, J Mater Chem A 2017, 5, 8933-8938.
[10]   J. Yan, M. T. F. Rodrigues, Z. Song, H. Li, H. Xu, H. Liu, J. Wu, Y. Xu, Y. Song, Y. Liu, Adv Funct Mater 2017, 27, 1700653.
[11]   W. Jiang, W. Luo, R. Zong, W. Yao, Z. Li, Y. Zhu, Small 2016, 12, 4370-4378.
[12]   H. Ou, P. Yang, L. Lin, M. Anpo, X. Wang, Angew Chem 2017, 56, 10905.
[13]   G. Zhang, J. Zhang, M. Zhang, X. Wang, J Mater Chem 2012, 22, 8083-8091.
[14]   G. Zhang, G. Li, Z. A. Lan, L. Lin, A. Savateev, T. Heil, S. Zafeiratos, X. Wang, M. Antonietti, Angew Chem Int Edit 2017, 56, 13445-13449.
[15]   Y. Wang, M. K. Bayazit, S. Moniz, Q. Ruan, C. C. Lau, N. Martsinovich, J. Tang, Energ Environ Sci 2017, 10, 1643-1651.

[16]   V. W.-h. Lau, I. Moudrakovski, T. Botari, S. Weinberger, M. B. Mesch, V. Duppel, J. Senker, V. Blum, B. V. Lotsch, Nat Commun 2016, 7, doi:10.1038/ncomms12165.

[17]   aQ. Cui, J. Xu, X. Wang, L. Li, M. Antonietti, M. Shalom, Angew Chem Int Edit 2016, 55, 3672-3676; bZ. Song, T. Lin, L. Lin, S. Lin, F. Fu, X. Wang, L. Guo, Angew Chem Int Edit 2016, 55, 2773-2777; cP. Xia, B. Zhu, J. Yu, S. Cao, M. Jaroniec, J Mater Chem A 2017, 5, 3230-3238.

[18]   aJ. Zhang, X. Chen, K. Takanabe, K. Maeda, K. Domen, J. D. Epping, X. Fu, M. Antonietti, X. Wang, Angew Chem Int Edit 2010, 49, 441-444; bG. Zhang, Z.-A. Lan, L. Lin, S. Lin, X. Wang, Chem Sci 2016, 7, 3062-3066; cY. S. Jun, E. Z. Lee, X. Wang, W. H. Hong, G. D. Stucky, A. Thomas, Adv Funct Mater 2013, 23, 3661-3667.

[19]   H. Tong, S. Ouyang, Y. Bi, N. Umezawa, M. Oshikiri, J. Ye, Adv Mater 2012, 24, 229-251.

[20]   aS. Guo, Z. Deng, M. Li, B. Jiang, C. Tian, Q. Pan, H. Fu, Angew Chem Int Edit 2016, 55, 1830-1834; bJ. Fang, H. Fan, Z. Zhu, L. B. Kong, L. Ma, J Catal 2016, 339, 93-101; cY. Kang, Y. Yang, L. C. Yin, X. Kang, L. Wang, G. Liu, H. M. Cheng, Adv Mater 2016, 28, 6471-6477.

[21]   aJ. Chen, C. L. Dong, D. Zhao, Y. C. Huang, X. Wang, L. Samad, L. Dang, M. Shearer, S. Shen, L. Guo, Adv Mater 2017, 29, DOI: 10.1002/adma.201606198; bC. Pan, J. Xu, Y. Wang, D. Li, Y. Zhu, Adv Funct Mater 2012, 22, 1518-1524.

[22]   aJ. Su, L. Guo, N. Bao, C. A. Grimes, Nano Lett 2011, 11, 1928-1933; bQ. Ruan, W. Luo, J. Xie, Y. Wang, X. Liu, Z. Bai, C. J. Carmalt, J. Tang, Angew Chem Int Edit 2017, 129, DOI: 10.1002/anie.201703372.